



Tailored design of PdRh bimetallic nanoribbons by solvent-induced strategy for efficient alkaline hydrogen evolution

Songliang Liu, Hugang Zhang, Hongjie Yu, Kai Deng, Ziqiang Wang, You Xu, Liang Wang, Hongjing Wang^{*}

State Key Laboratory Breeding Base of Green-Chemical Synthesis Technology, College of Chemical Engineering, Zhejiang University of Technology, Hangzhou 310014, PR China

ARTICLE INFO

Keywords:

PdRh
Bimetallic
Nanoribbons
Solvent-induced strategy
Hydrogen evolution reaction

ABSTRACT

Metallene with unusual physicochemical properties is a very promising class of two-dimensional electrocatalyst for efficient electrochemical hydrogen production. However, the controllable construction of metallene in the extension direction remains a great challenge. Herein, PdRh bimetallics (PdRh BMs) and PdRh bimetallic nanoribbons (PdRh BNRs) were controllably prepared by solvent-induced strategy for efficient hydrogen evolution. The overpotential required for PdRh BNRs to reach 10 mA cm^{-2} at 1 M KOH is only 32 mV, which is better than PdRh BMs and Pd metallene nanoribbons. Aberration-corrected HRTEM revealed abundant defects on the surface of PdRh BNRs, which not only act as high active sites but also generate strong strain to significantly reduce the *d*-band center of Pd. This work provides guidance for the construction of high efficiency catalysts in metallene by applying defect engineering and strain engineering, and also provides a novel strategy for the controllable extension of metallene in longitudinal dimension.

1. Introduction

The rapid development of electricity generation from renewable energy (solar and wind energy, etc.) has reduced the cost of electricity and further accelerated the commercial application in electrocatalytic conversion [1–3]. Among them, electrically driven electrochemical water splitting is one of the most promising ways to generate green and high-purity hydrogen [4–7]. Hydrogen evolution reaction (HER) is a cathodic process of electrochemical water splitting, and the exploration of efficient catalysts for HER process plays an indispensable role in the development of hydrogen-based energy [8–11]. Industrial HER is generally in alkaline medium, and Pd-based catalysts have been widely used in alkaline HER [12–15]. However, the slow kinetics of the water dissolution step ($\text{H}_2\text{O} \rightarrow \text{H}^+ + \text{OH}^-$) and poor catalytic stability still hinder the large-scale commercial application of Pd-based catalysts [16–18]. Therefore, there is an urgent need to develop an efficient and stable Pd-based alkaline HER catalyst.

It has been shown that adjusting the coordination state and electron configuration of Pd by alloying Pd with other metals (Pb, Rh, Cu, Ir, etc.) is one of the effective strategies to improve the catalytic performance [19–22]. Among them, Rh is very stable in alkaline media due to its high

redox potential, and further alloying with Pd can significantly enhance the catalytic stability and provide more catalytic active sites [23–27]. Therefore, PdRh alloy will become a promising catalyst candidate for alkaline HER. In addition, the catalytic performance is closely related to the morphological structure of the catalyst, and the structural engineering strategy is another effective way to optimize catalytic performance [28–31]. Atomically thin two-dimensional (2D) structure has the characteristics of large specific surface area, high atomic utilization, and abundant active sites, among which the excellent performance of metallene (a class of single-layer metal nanosheets with graphene-like morphology) in the field of electrocatalysis has attracted widespread attention. [32–37] However, precise control of the longitudinal extension of metallene into nanoribbon structures at the atomic level remains a huge challenge. [38,39]. 2D metallene and metallene nanoribbons will provide ideal models for designing advanced catalysts at the atomic level due to their unique atomically thin structures. In addition to the composition and morphology regulation, structural defect construction can induce the generation of strain effect and provide additional catalytic active sites to enhance the catalytic performance [40–44]. For example, Guo and co-authors successfully prepared Pd metallene with atomic-level cavities through defect engineering, and the atomic-level

^{*} Corresponding author.

E-mail address: hjw@zjut.edu.cn (H. Wang).

<https://doi.org/10.1016/j.apcatb.2023.122948>

Received 9 April 2023; Received in revised form 26 May 2023; Accepted 31 May 2023

Available online 1 June 2023

0926-3373/© 2023 Elsevier B.V. All rights reserved.

cavity with high coordination defects significantly regulated the coordination environment of the catalytic active site, thus regulating the adsorption energy and kinetics of the reaction [45]. Based on the above analysis, the ingenious introduction of structural defects into metallene and metallene nanoribbons has leading significance for structural design of electrocatalyst and optimization of catalytic performance.

Herein, we propose a solvent-induced strategy for the controllable preparation of atomically thin and defect-rich PdRh bimetalenes (PdRh BMs) and PdRh bimetalene nanoribbons (PdRh BNRs). When the as-prepared PdRh BMs and PdRh BNRs are used in alkaline HER, the PdRh BNRs with rich atom channels show better HER performance. Density functional theory (DFT) studies further confirm that the electron configuration of Pd metallene nanoribbons (Pd MNRs) can be regulated by the introduction of Rh element, and the strain effect caused by structural defects significantly reduces the *d*-band center, thus obtaining better catalytic activity and stability. This work proposes the controllable preparation of metallene and metallene nanoribbons by a solvent-induced strategy, which provides ideal catalyst templates for the field of energy electrocatalysis.

2. Experimental section

2.1. Materials and chemicals

Na_2PdCl_4 , $\text{RhCl}_3 \cdot x\text{H}_2\text{O}$, $\text{Mo}(\text{CO})_6$, polyvinyl pyrrolidone (PVP, $M_w = 40000$), L-ascorbic acid (AA), $\text{Fe}_2(\text{CO})_9$, $\text{Co}_2(\text{CO})_8$, $\text{W}(\text{CO})_6$, $\text{Cr}(\text{CO})_6$ were provided from Aladdin. Ethanediamine (EN), diethylenetriamine (DETA), N-N-Dimethylacetamide (DMAC), N,N-Dimethylformamide (DMF), ethanol and acetone were purchased from Beijing Chemical Works.

2.2. Synthesis of the PdRh BMs and PdRh BNRs

For a typical synthesis of PdRh BNRs, AA (80 mg), $\text{Mo}(\text{CO})_6$ (50 mg) and PVP (600 mg) were added to 2 mL of DETA to dissolve ultrasonically. Subsequently, 0.49 mL $\text{RhCl}_3 \cdot x\text{H}_2\text{O}$ (0.1 M) and 0.01 mL Na_2PdCl_4 (0.1 M) were added to the above clarified solution, and then put it in an oil bath at 120 °C for 8 h. Finally, the PdRh BNRs are washed 5 times by centrifugation with acetone, water, and ethanol. PdRh BMs was prepared by replacing EDTA with EN under typical conditions.

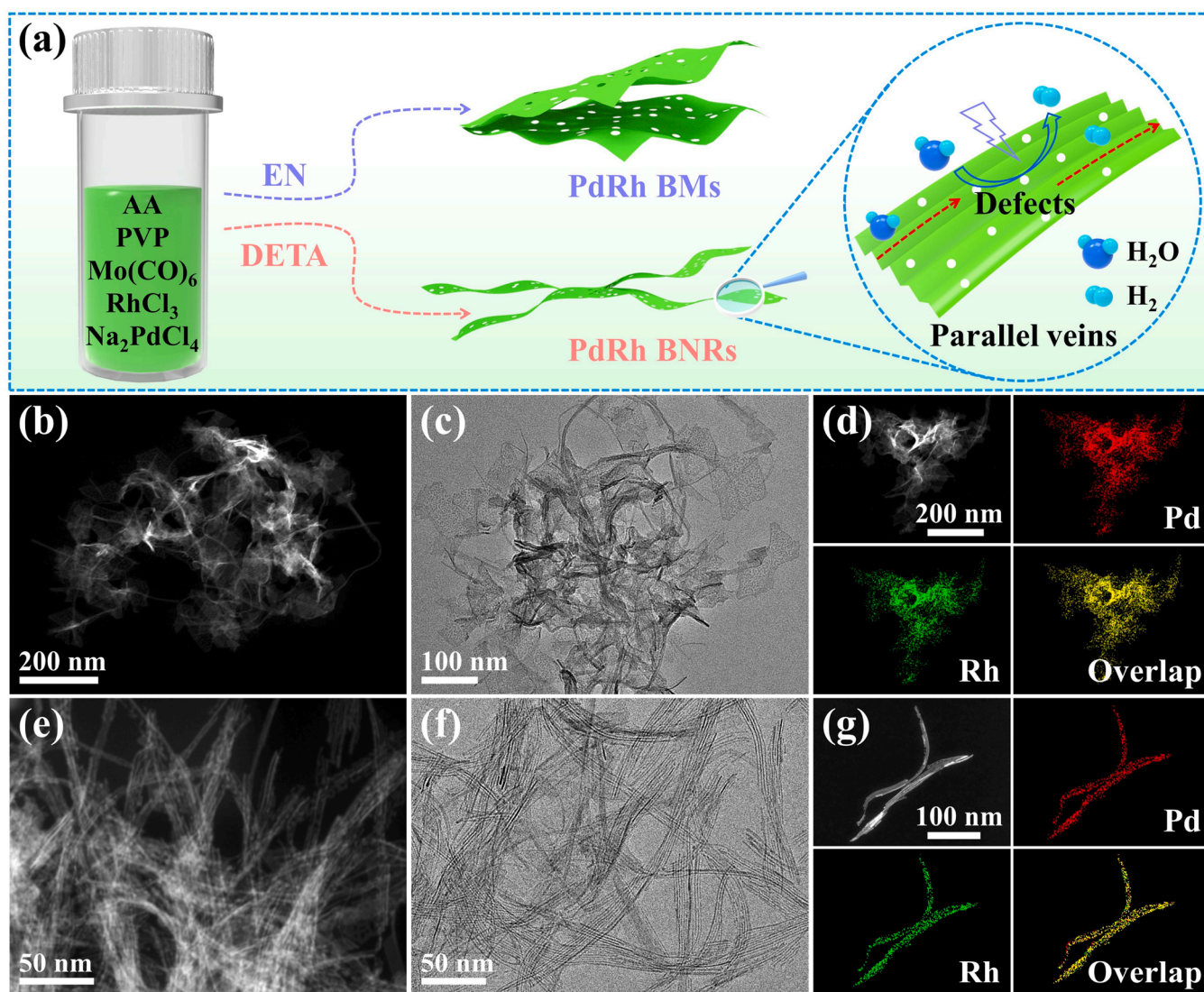


Fig. 1. (a) Schematic illustration for the synthesis of PdRh BMs and PdRh BNRs by solvent-induced strategy. (b) HAADF-STEM and (c) TEM images of the PdRh BMs. (d) HAADF-STEM and EDX mapping images of the PdRh BMs. (e) HAADF-STEM and (f) TEM images of the PdRh BNRs. (g) HAADF-STEM and EDX mapping images of the PdRh BNRs.

2.3. Synthesis of the Pd MNRs

Pd MNRs were prepared by replacing $\text{RhCl}_3 \cdot x\text{H}_2\text{O}$ with Na_2PdCl_4 under typical conditions.

3. Results and discussion

3.1. Synthesis and characterization of the PdRh BMs and PdRh BNRs

Fig. 1a illustrates two different evolution processes when DETA and EN are used as the reaction solvents, respectively. In a typical synthesis of PdRh alloys with different morphology, Na_2PdCl_4 , $\text{RhCl}_3 \cdot x\text{H}_2\text{O}$, AA, PVP and $\text{Mo}(\text{CO})_6$ were mixed in different solvents and heated at 120°C for 8 h. EN and DETA as reaction solvents for the selective generation of PdRh BMs and PdRh BNRs, respectively. High-angle annular dark-field scanning transmission electron microscopy (HAADF-STEM) images and transmission electron microscopy (TEM) images show that the PdRh BMs synthesized using EN exhibit high yields of graphene nanosheet-like structure and possess many wrinkles (Figs. 1b and 1c). When DETA is used as the reaction solvent, the as-prepared PdRh BNRs exhibit uniform ultrathin nanoribbon structure, realizing the controlled longitudinal extension of PdRh BMs (Figs. 1e and 1f). The HAADF-STEM images and the corresponding energy dispersive X-ray spectroscopy (EDX) images reveal the uniformly distribution of Pd and Rh in the metallene and metallene nanoribbons (Figs. 1d and 1g). EDX analysis reveals that the atomic ratios of Pd/Rh in PdRh BMs and PdRh BNRs are about 5/1 and 17/3, respectively (Fig. S1).

The PdRh BMs and PdRh BNRs were characterized in detail. High-magnification HAADF-STEM and TEM images show that the surface of PdRh BMs has a large number of pores, and the average thickness is 1.4 nm (Figs. 2a, b, d and S2a). In addition, the average thickness of PdRh BMs measured by atomic force microscopy (AFM) is also 1.4 nm, which further demonstrated the formation 2D ultrathin nanosheet-like structure (Fig. 2c). The selected electron diffraction (SAED) pattern reveals a clear concentric ring profile, indicating that the PdRh BMs are polycrystalline (Fig. 2d). HRTEM images and aberration-corrected HAADF-STEM images show that the PdRh BNRs are face-centered

cubic (fcc) phase and mainly consist of (111) crystal planes (Fig. 2e and S2b). In addition, PdRh BMs have abundant structural defects, such as atomic step, twin boundary, and vacancy defects (Figs. 2e, 2f and S2b). The obtained PdRh BNRs are uniform ultrathin nanoribbon structures with a length of several hundred nanometers and a width of about 24 nm, and the surface has abundant parallel veins and wrinkles (Figs. 3a, c and S2c). The ordered parallel veins not only increase the specific surface area, but also become the channel of atom transfer to further promote the mass transfer process. The average thickness of PdRh BNRs is 1.4 nm by AFM test, which is similar to that of PdRh BMs, further confirming that the PdRh BNRs is atomically thin nanoribbon structure (Fig. 3b and S3). The SAED pattern presents concentric rings similar to that of PdRh BMs (Fig. S2c). HRTEM images and aberration-corrected HAADF-STEM images further confirm that PdRh BMs have lattice fringes with a lattice spacing of 0.230 nm, which can correspond to the (111) plane of fcc PdRh alloy (Figs. 3d, 3e and S2d). Abundant structural defects can be observed on the surface and edge of PdRh BNRs (Figs. 3d, 3e and S2d). The lattice spacing of Pd metallene nanoribbons (Pd MNRs) with smooth and defect-free surfaces is 0.225 nm, corresponding to the (111) surface of fcc Pd (Fig. S4). According to the tensile strain formula $\tau = (\alpha_{\text{PdRh BNRs}} - \alpha_{\text{Pd MNRs}}) / \alpha_{\text{Pd MNRs}}$, the tensile strain of PdRh BNRs to Pd MNRs is 2.2% [46–48]. The results show that the introduction of structural defects can generate lattice strain to optimize the electron configuration between atoms, further accelerate the charge transfer and enhance the mass transfer process.

The crystal structure of the prepared samples was characterized by X-ray diffraction (XRD). The XRD patterns of all samples showed obvious diffraction peaks of fcc structure (Fig. 3f). In addition, the peak positions of both PdRh BMs and PdRh BNRs were shifted negatively compared with the Pd MNRs without Rh element introduced, confirming the formation of PdRh alloy [49]. XPS results show that Pd and Rh elements in PdRh BMs and PdRh BNRs mostly exist in metallic state (Fig. 3g). In addition, a small amount of Pd(II) species exists in the Pd 3d XPS spectrum, which may be attributed to the partial oxidation of PdRh BMs and PdRh BNRs in air [29,50]. Compared with the Pd MNRs, the Pd 3d binding energy of PdRh BMs and PdRh BNRs both shifted to a certain extent in the negative direction, which indicated that the introduction of

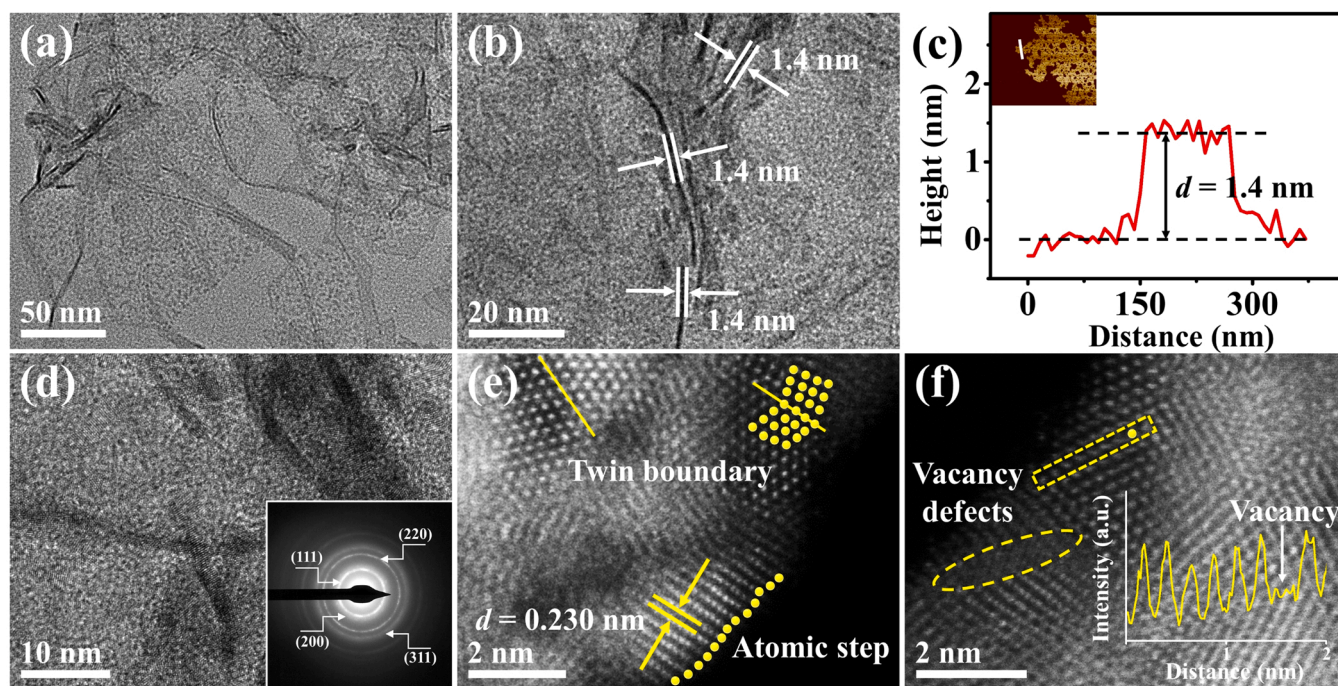


Fig. 2. (a and b) TEM images of the PdRh BMs. (c) AFM image and corresponding height profile of the PdRh BMs. (d) TEM and SAED images of the PdRh BMs. (e and f) Aberration-corrected HAADF-STEM of the PdRh BMs. The inset in (f) is intensity profile of the yellow square area in (f).

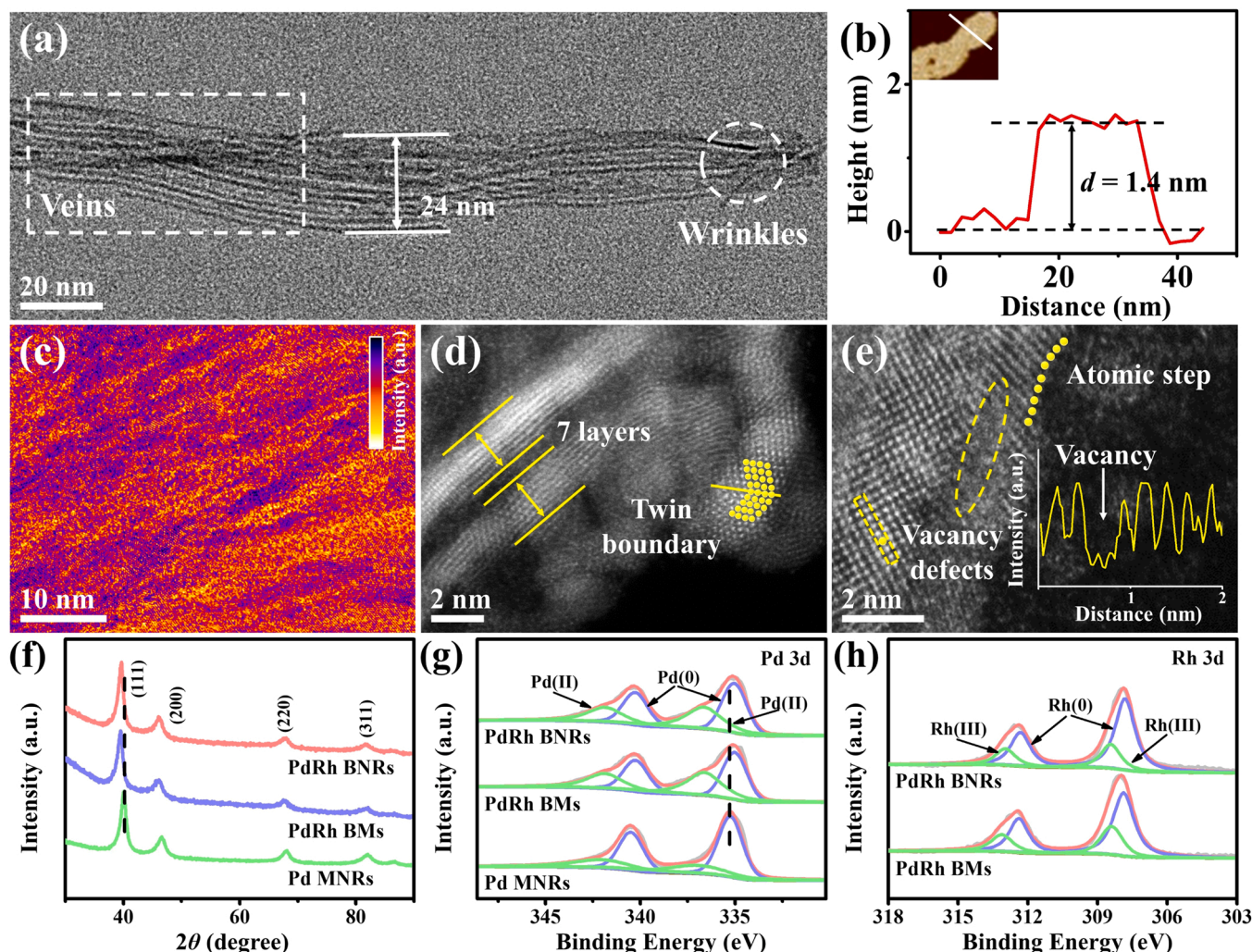


Fig. 3. (a) TEM image of the PdRh BNRs. (b) AFM image and corresponding height profile of the PdRh BNRs. (c) False-color HRTEM image and (d and e) aberration-corrected HAADF-STEM images of the PdRh BNRs. The inset in (e) is intensity profile of the yellow square area in (e). (f) XRD patterns and (g) XPS spectra of the Pd 3d peaks of Pd MNRs, PdRh BMs and PdRh BNRs. (h) XPS spectra of the Rh 3d peaks of PdRh BMs and PdRh BNRs.

Rh element led to the transfer of electrons from Rh to Pd, thereby optimizing the electronic configuration of Pd [50]. This optimized electron configuration can facilitate the desorption of products and accelerate the transport of electrons. In the Rh 3d XPS spectrum, two obvious doublets can be observed, which can be attributed to Rh 3d_{3/2} and Rh 3d_{5/2}, respectively (Fig. 3h). The peak positions at 312.3 and 307.7 eV can be assigned to Rh(0), and the two peaks at 313.2 and 308.8 eV can be assigned to Rh(III).

The formation mechanism of PdRh BNRs was studied by adjusting the synthesis parameters of PdRh BNRs. Pd MNRs with wider size were obtained in DETA system without adding Rh precursor (Fig. S4). When EN is used as a solvent without adding Rh precursor, narrower Pd nanoribbons with different sizes can be obtained (Fig. S5). The results show that Rh precursor can regulate the size and uniformity of nanoribbons. In addition, we found that PVP and AA were essential in the formation of 2D nanoribbons. When PVP is not added, only the agglomeration and non-uniform nanoribbons can be obtained, while excessive PVP can only obtain narrow PdRh nanoribbons (Fig. S6). When no AA is added, only scattered small particles can be obtained, and excessively agglomerated nanoribbons can be obtained with excessive AA (Fig. S7). Carbonyl reagents can be pyrolyzed to produce CO, thus acting as reducing agents and structure guiding agents [23–27]. In order to study the role of Mo(CO)₆ in the synthesis, we use the same type of carbonyl reagent (W(CO)₆, Co₂(CO)₈, Fe₂(CO)₉, Cr(CO)₆)

replaced of Mo(CO)₆. The results show that the same type of carbonyl reagents could not obtain the nanoribbon structure, so Mo(CO)₆ is irreplaceable in the process of synthesizing nanoribbons (Fig. S8). In terms of solvent selection, in addition to using EN instead of DETA to synthesize Pd MNRs, similar amines DMF and DMAC are used instead of DETA, but only irregular nanoparticle structures can be synthesized (Fig. S9). Therefore, the selection of appropriate solvents can induce the controlled longitudinal extension of metallene, which is an indispensable factor during the formation of metallene nanoribbon.

In order to further understand the synthesis mechanism of PdRh BNRs, TEM images of intermediates with different reaction time intervals were collected. Fig. 4 reveals the growth of PdRh BNRs. During the initial stage of the reaction (5 min), shorter nanowire structures are formed (Fig. 4b). Short and narrow nanoribbon structures began to appear as the reaction time extended to 10 min and 30 min (Figs. 4d and 4f). When the reaction time is extended to 1 h, the longitudinal and transverse dimensions of the nanoribbons are further extended, and a uniform nanoribbon structure is gradually formed (Fig. 4e). The typical reaction time of PdRh BNRs is 8 h, which enables the metal precursor can be reacted more completely (Fig. 4g). From the above results, the potential formation mechanism of PdRh BNRs can be obtained. First, the metal precursors (Pd²⁺, Rh³⁺) rapidly chelate with DETA to form a coordination complex, which is quickly adsorbed by surfactant PVP. With the progress of reaction time, Mo(CO)₆ slowly decomposed to form CO

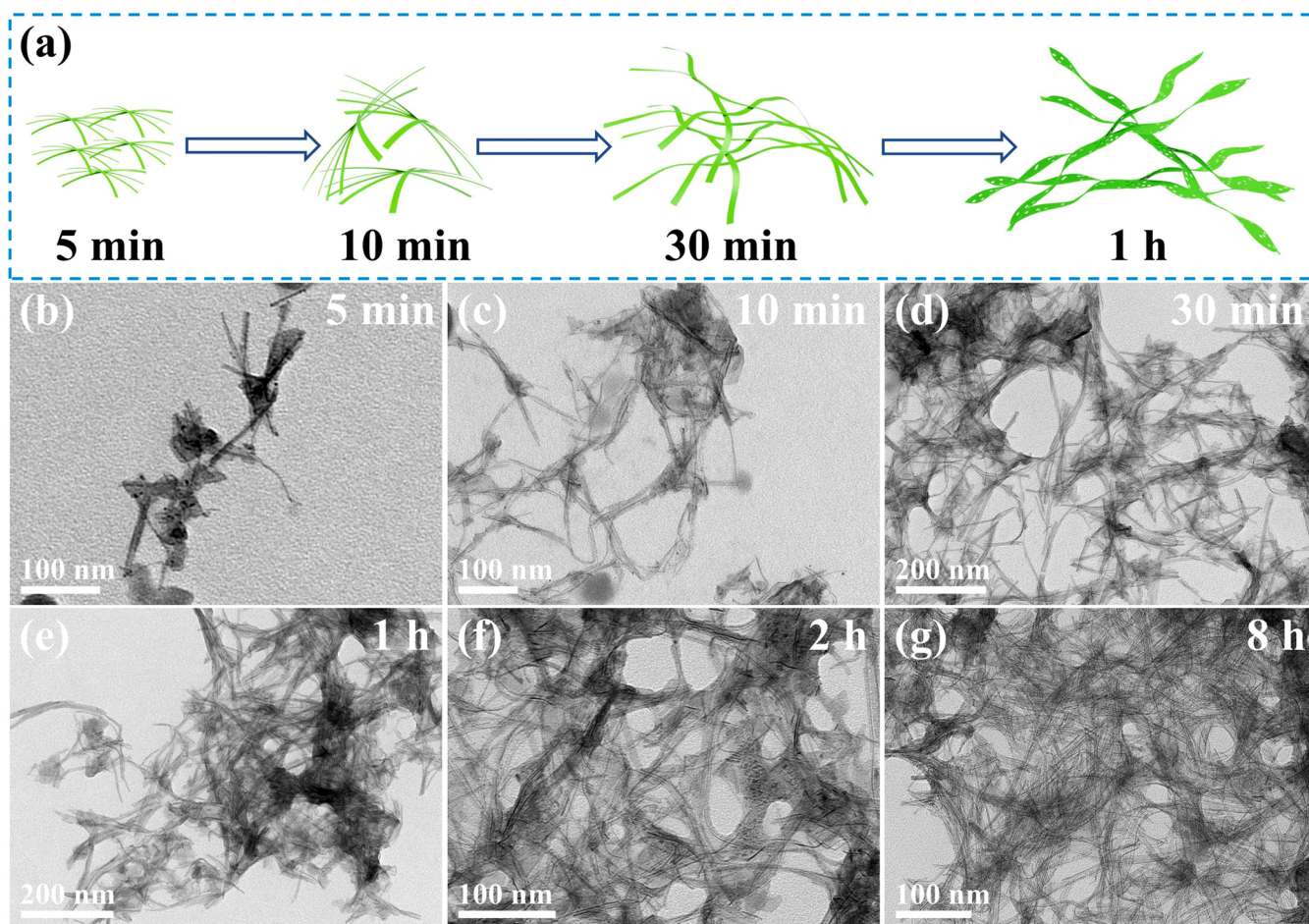


Fig. 4. (a) Geometric models, TEM images of the prepared samples at different reaction times under the typical synthesis conditions: (b) 5 min, (c) 10 min, (d) 30 min, (e) 1 h, (f) 2 h and (g) 8 h.

and quickly adsorbed on the (111) crystal planes of the metal precursor, thus acting as a 2D structure guide agent. Finally, under the reduction of reducing agents AA and CO, the metal precursors are slowly reduced with the assistance of PVP and CO to gradually form nanoribbon structures.

3.2. Electrocatalytic performances for HER

The alkaline HER performance of PdRh BNRs was evaluated in 1 M KOH using a three-electrode system, in which PdRh BMs, Pd MNRs and commercial catalysts (Pt/C) were tested as benchmarks (Fig. S10). As shown in the linear sweep voltammetry (LSV) curves in Fig. 5a, compared with the benchmark catalyst, the PdRh BNRs showed the best HER performance. Impressively, it only requires an overpotential of 32 mV to achieve a cathode current density of $\sim 10 \text{ mA cm}^{-2}$, which was significantly lower than that of PdRh BMs (44 mV), Pd MNRs (183 mV) and Pt/C (57 mV) (Fig. 5b). The excellent HER activity of PdRh BNRs is mainly derived from the exposure of a large number of structural defects and the introduction of Rh element optimized the electronic configuration of Pd. In addition, the HER reaction kinetics of PdRh BNRs were further investigated using Tafel plots. The Tafel slope of PdRh BNRs (51 mV dec^{-1}) was smaller than that of PdRh BMs (58 mV dec^{-1}), Pd MNRs (119 mV dec^{-1}) and commercial Pt/C (60 mV dec^{-1}), indicating that PdRh BNRs had the best HER kinetics (Fig. 5c). The Tafel slope of PdRh BNRs (51 mV dec^{-1}) indicated that the HER process followed the Volmer–Heyrovsky mechanism (Fig. 5g). Notably, PdRh BNRs also exhibited better HER activity than recently reported noble metal-based HER electrocatalysts (Table S1).

The charge transfer on the PdRh BNRs interface was further investigated by electrochemical impedance spectroscopy (EIS) (Fig. 5d). The impedance spectrum profile of PdRh BNRs showed the smallest semi-circle corresponding to the lowest charge transfer resistance (R_{ct}), which was significantly smaller than that of PdRh BMs, Pd MNRs and Pt/C, indicating faster electronic conductivity on PdRh BNRs. The faster charge transfer was mainly derived from the abundant parallel vein structure on the surface of PdRh BNRs and the introduction of Rh element to optimize the charge distribution of Pd atoms. In addition, the electrochemical active surface area (ECSA) of various catalysts were measured using CO stripping experiments (Fig. S11). The ECSA of PdRh BNRs was $72.1 \text{ m}^2 \text{ g}^{-1}$, which was significantly higher than that of PdRh BMs ($64.4 \text{ m}^2 \text{ g}^{-1}$), Pd MNRs ($56.2 \text{ m}^2 \text{ g}^{-1}$) and Pt/C ($45.6 \text{ m}^2 \text{ g}^{-1}$), indicating that PdRh BNRs could provide more catalytic activity for HER process (Fig. S12). Fig. 5e showed that the HER polarization curve of PdRh BNRs after 10,000 cycles almost overlaps with the initial polarization curve, indicating the excellent HER stability of PdRh BNRs. At the same time, the 20 h V-t test was performed under the overpotential of $\sim 10 \text{ mA cm}^{-2}$, the V-t curve of PdRh BNRs only slightly fluctuated and almost decayed, which was far better than that of commercial Pt/C (Fig. 5f). This further indicates the excellent long-term HER stability of PdRh BNRs. After the V-t test for 20 h, the structure of PdRh BNRs remained intact and the metallene nanoribbon structure without collapse (Fig. S13).

In order to elucidate the mechanism of PdRh BNRs enhancing HER performance, we established the geometric structure models of PdRh BNRs and Pd MNRs by density functional theory (DFT) (Figs. 6a and b). Bader charge analysis showed that the total net charge of Pd was

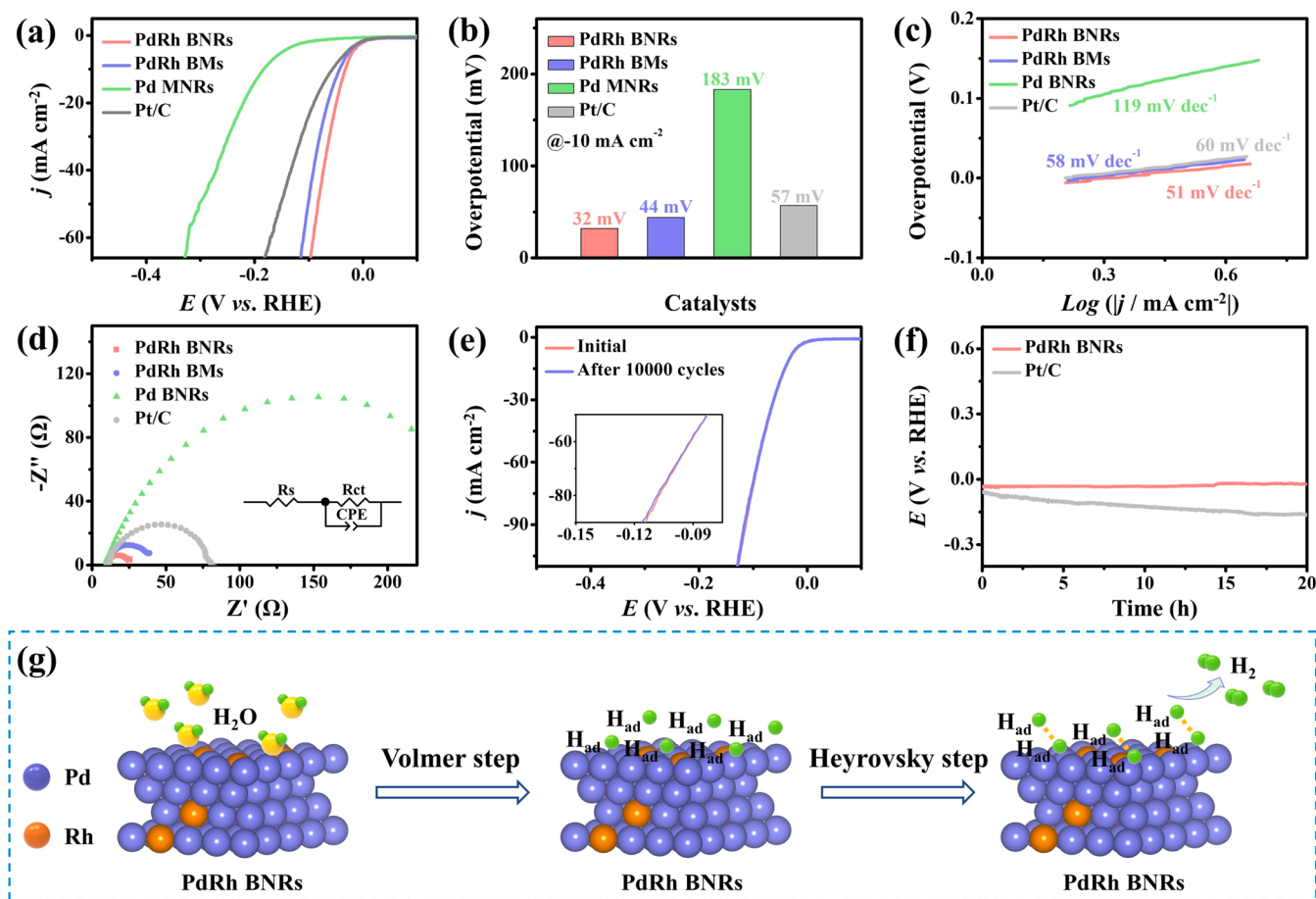


Fig. 5. (a) HER polarization curves of various catalysts in 1 M KOH, and (b) the comparison of overpotentials at @ -10 mA cm^{-2} . (c) Tafel slope plots and (d) EIS curves for various catalysts. (e) HER polarization curves of the PdRh BNRs before and after 10000 cycles in 1 M KOH. (f) Chronopotentiometry curves of Pt/C and PdRh BNRs at a continuous cathodic current density of @ -10 mA cm^{-2} in 1 M KOH for 20 h. (g) Schematic HER mechanism of PdRh BNRs.

negative and that of Rh was positive, thus confirming that the introduction of Rh made electrons transfer from Rh atom to Pd atom (Figs. 6c-e and S14). This result indicates that the introduction of Rh can make the surrounding Pd atoms acquire electrons and thus exhibit negative charge properties, which is conducive to the adsorption of free protons in water, which is consistent with the XPS results. The projected density of states (PDOS) of Pd d -band was obtained through simulation calculation. The d -band center of PdRh BNRs (-1.78 eV) was significantly decreased compared with Pd MNRs (-1.67 eV), further indicating that the introduction of Rh element can reduce d -band center thus facilitate the desorption process of the product H_2 and releases the active sites (Fig. 6f). In addition, we further calculated the H_2O adsorption and dissociation, and the hydrogen adsorption free energy (ΔG_{H^*}) to evaluate the HER activity of PdRh BNRs (Figs. 6g-h). The water adsorption energy and dissociation energy of different sites in PdRh BNRs were studied, the Rh site in PdRh BNRs showed the best H_2O adsorption energy and the Pd site in PdRh BNRs showed the best dissociation energy (Fig. 6g, h and S15). The above results indicated that the introduction of Rh can optimize H_2O adsorption and dissociation. The higher the ΔG_{H^*} , the weaker the hydrogen adsorption. The ΔG_{H^*} value of Pd sites and Rh sites in PdRh BNRs and the comparative sample Pd sites in Pd MNRs and Pt sites in Pt/C was studied (Fig. 6i and S16) [51]. Compared with other sites, the ΔG_{H^*} value of Pd site in PdRh BNRs was the closest to HER optimal standard ($\Delta G_{\text{H}^*} = 0$), indicated that Pd site can obtain the best HER activity in PdRh BNRs [51,52]. The above results indicate that the introduction of Rh element optimizes the electronic structure around the Pd atom and promotes the optimal Pd-H binding at the Pd site, thereby accelerating the H^* adsorption and H_2 release process.

Overall, by choosing different solvents to adjust the adsorption energy and reaction rate of the precursor, the controllable extension of Pd nanocrystalline longitudinal dimension was obtained. Benefiting from the advantages of defect engineering and strain engineering, the obtained PdRh BNRs exhibit excellent performance of alkaline electrocatalytic hydrogen production. On the one hand, atomically thin PdRh BNRs have abundant structural defects and parallel veins, which can expose more surface atoms and provide more atom transfer channels, thus accelerating the mass transfer process. In addition, the metallene nanoribbon structure has excellent structural stability, which can effectively prevent the agglomeration and deactivation of the catalyst and thus enhance the catalytic stability. On the other hand, the introduction of Rh element and the strain effect caused by structural defects can optimize the electron density around Pd and reduce its d -band center, thereby achieving the effect of activating molecules and accelerating the desorption of reactants.

4. Conclusion

In summary, we propose a solvent-induced strategy to successfully construct atomically thin PdRh BMs and PdRh BNRs, and achieve controllable extension of the metallene in the longitudinal dimension. Thanks to the incorporation of Rh atoms and the highly strained atom-rich channel metallene nanoribbon structure, the developed PdRh BNRs exhibit excellent HER catalytic activity (Overpotential 32 mV at 10 mA cm^{-2}) and stability under alkaline conditions. DFT confirm that the introduction of Rh atoms and the construction of defects can effectively optimize the electron density of Pd, thereby enhancing the HER

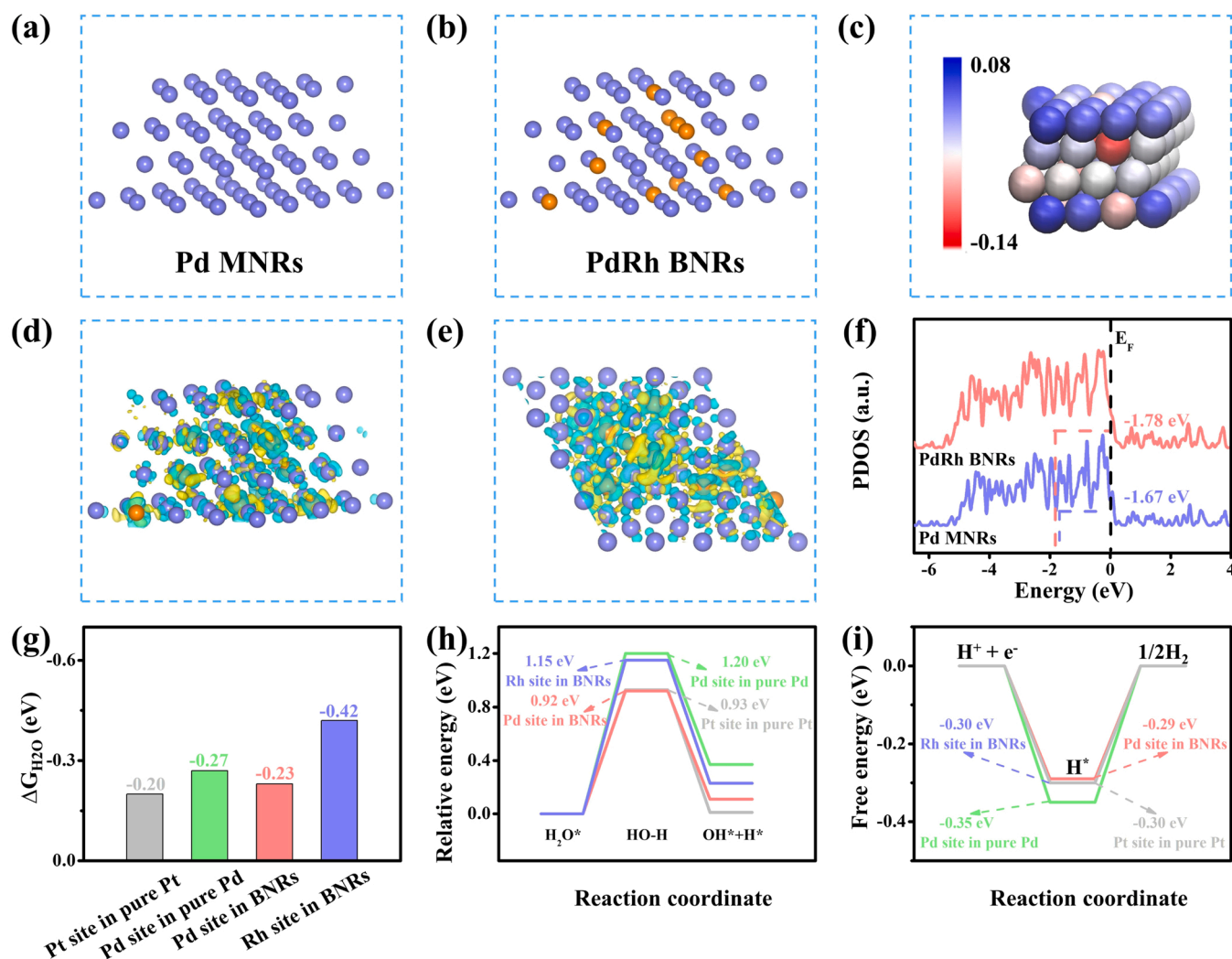


Fig. 6. The geometric structure models for (a) Pd MNRs and (b) PdRh BNRs. (c) Bader charge of the PdRh BNRs. Negative and positive charge are indicated by red and blue balls, respectively. (d) Electron density difference on the PdRh BNRs. (e) Top-view of electron density difference on the PdRh BNRs. (f) The PDOS of Pd MNRs and PdRh BNRs. The calculated (g) adsorption free energy of water, (h) energy profile for water dissociation and (i) free energy profiles of HER for two representative sites on the surfaces of PdRh BNRs, Pd site on pure Pd (111) and Pt site on pure Pt (111).

performance. This work not only provides an idea for the design of electrocatalysts with high catalytic performance, but also opens a novel strategy for the controllable extension of metallene in the longitudinal dimension.

CRediT authorship contribution statement

Songliang Liu: Experimental Measurements, Data Analysis, Manuscript Preparation. **Hugang Zhang:** Experimental Measurements, Data Analysis. **Hongjie Yu:** Data Analysis. **Kai Deng:** Experimental Measurements. **Ziqiang Wang:** Conceptualization, Funding acquisition. **You Xu:** Reviewing and Editing. **Liang Wang:** Reviewing and Editing, Supervision, Project administration. **Hongjing Wang:** Conceptualization, Reviewing and Editing, Supervision, Project administration.

Declaration of Competing Interest

The authors declare that they have no known competing financial interests or personal relationships that could have appeared to influence the work reported in this paper.

Data Availability

Data will be made available on request.

Acknowledgement

This work was financially supported by the National Natural Science Foundation of China (No. 21972126, 21978264, 21905250, 22278369), Natural Science Foundation of Zhejiang Province (No. LQ22B030012 and LQ23B030010) and China Postdoctoral Science Foundation (2021M702889).

Appendix A. Supporting information

Supplementary data associated with this article can be found in the online version at [doi:10.1016/j.apcatb.2023.122948](https://doi.org/10.1016/j.apcatb.2023.122948).

References

- [1] M. Chatenet, B.G. Pollet, D.R. Dekel, F. Dionigi, J. Deseure, P. Millet, R.D. Braatz, M.Z. Bazant, M. Eikerling, I. Staffell, P. Balcombe, Y. Shao-Horn, H. Schäfer, Water electrolysis: from textbook knowledge to the latest scientific strategies and industrial developments, *Chem. Soc. Rev.* 51 (2022) 4583–4762, <https://doi.org/10.1039/d0cs01079k>.

- [2] J.N. Tiwari, S. Sultan, C.W. Myung, T. Yoon, N. Li, M. Ha, A.M. Harzandi, H. J. Park, D.Y. Kim, S.S. Chandrasekaran, W.G. Lee, V. Vij, H. Kang, T.J. Shin, H. S. Shin, G. Lee, Z. Lee, K.S. Kim, Multicomponent electrocatalyst with ultralow Pt loading and high hydrogen evolution activity, *Nat. Energy* 3 (2018) 773–782, <https://doi.org/10.1038/s41560-018-0209-x>.
- [3] Y. Yin, Y. Zhang, T. Gao, T. Yao, X. Zhang, J. Han, X. Wang, Z. Zhang, P. Xu, P. Zhang, X. Cao, B. Song, S. Jin, Synergistic phase and disorder engineering in 1T-MoSe₂ nanosheets for enhanced hydrogen-evolution reaction, *Adv. Mater.* 29 (2017) 1700311, <https://doi.org/10.1002/adma.201700311>.
- [4] J. Xu, I. Amorim, Y. Li, J. Li, Z. Yu, B. Zhang, A. Araujo, N. Zhang, L. Liu, Stable overall water splitting in an asymmetric acid/alkaline electrolyzer comprising a bipolar membrane sandwiched by bifunctional cobalt-nickel phosphide nanowire electrodes, *Carbon Energy* 2 (2020) 646–655, <https://doi.org/10.1002/cey2.56>.
- [5] B. You, X. Liu, N. Jiang, Y. Sun, A general strategy for decoupled hydrogen production from water splitting by integrating oxidative biomass valorization, *J. Am. Chem. Soc.* 138 (2016) 13639–13646, <https://doi.org/10.1021/jacs.6b07127>.
- [6] Y. Li, P. Kidkhunthod, Y. Zhou, X. Wang, J.M. Lee, Dense heterointerfaces and unsaturated coordination synergistically accelerate electrocatalysis in Pt/Pt₅P₂ porous nanocages, *Adv. Funct. Mater.* 32 (2022) 2205985, <https://doi.org/10.1002/adfm.202205985>.
- [7] B. Ni, Q. Zhang, C. Ouyang, S. Zhang, B. Yu, J. Zhuang, L. Gu, X. Wang, The synthesis of sub-nano-thick Pd nanobelt-based materials for enhanced hydrogen evolution reaction activity, *CCS Chem.* 2 (2020) 642–654, <https://doi.org/10.31635/ccschem.019.201900054>.
- [8] W. Song, M. Li, C. Wang, X. Lu, Electronic modulation and interface engineering of electropun nanomaterials-based electrocatalysts toward water splitting, *Carbon Energy* 3 (2020) 101–128, <https://doi.org/10.1002/cey2.85>.
- [9] Z.-L. Wang, K. Sun, J. Henzie, X. Hao, C. Li, T. Takei, Y.-M. Kang, Y. Yamauchi, Spatially confined assembly of monodisperse ruthenium nanoclusters in a hierarchically ordered carbon electrode for efficient hydrogen evolution, *Angew. Chem., Int. Ed.* 57 (2018) 5848–5852, <https://doi.org/10.1002/anie.201801467>.
- [10] K. Wang, B. Huang, F. Lin, F. Lv, M. Luo, P. Zhou, Q. Liu, W. Zhang, C. Yang, Y. Tang, Y. Yang, W. Wang, H. Wang, S. Guo, Wrinkled Rh₂P nanosheets as superior pH-universal electrocatalysts for hydrogen evolution catalysis, *Adv. Energy Mater.* 8 (2018) 1801891, <https://doi.org/10.1002/aenm.201801891>.
- [11] Y. Guo, J. Tang, Z. Wang, Y.-M. Kang, Y. Bando, Y. Yamauchi, Elaborately assembled core-shell structured metal sulfides as a bifunctional catalyst for highly efficient electrochemical overall water splitting, *Nano Energy* 47 (2018) 494–502, <https://doi.org/10.1016/j.nanoen.2018.03.012>.
- [12] T. Jiang, L. Yu, Z. Zhao, W. Wu, Z. Wang, N. Cheng, Regulating the intermediate affinity on Pd nanoparticles through the control of inserted-B atoms for alkaline hydrogen evolution, *Chem. Eng. J.* 433 (2022), 133525, <https://doi.org/10.1016/j.cej.2021.133525>.
- [13] D. Zhang, H. Zhao, B. Huang, B. Li, H. Li, Y. Han, Z. Wang, X. Wu, Y. Pan, Y. Sun, X. Sun, J. Lai, L. Wang, Advanced ultrathin RuPdM (M = Ni, Co, Fe) nanosheets electrocatalyst boosts hydrogen evolution, *ACS Cent. Sci.* 5 (2019) 1991–1997, <https://doi.org/10.1021/acscentsci.9b01110>.
- [14] Z. Lin, B. Xiao, Z. Wang, W. Tao, S. Shen, L. Huang, J. Zhang, F. Meng, Q. Zhang, L. Gu, W. Zhong, Planar-coordination PdSe₂ nanosheets as highly active electrocatalyst for hydrogen evolution reaction, *Adv. Funct. Mater.* 31 (2021) 2102321, <https://doi.org/10.1002/adfm.202102321>.
- [15] N. Mahmood, Y. Yao, J.-W. Zhang, L. Pan, X. Zhang, J.-J. Zou, Electrocatalysts for hydrogen evolution in alkaline electrolytes: mechanisms, challenges, and prospective solutions, *Adv. Sci.* 5 (2018) 1700464, <https://doi.org/10.1002/advs.201700464>.
- [16] B. Zhang, G. Zhao, B. Zhang, L. Xia, Y. Jiang, T. Ma, M. Gao, W. Sun, H. Pan, Lattice-confined Ir clusters on Pd nanosheets with charge redistribution for the hydrogen oxidation reaction under alkaline conditions, *Adv. Mater.* 33 (2021) 2105400, <https://doi.org/10.1002/adma.202105400>.
- [17] G. Sheng, J. Chen, Y. Li, H. Ye, Z. Hu, X.-Z. Fu, R. Sun, W. Huang, C.-P. Wong, Flowerlike NiCo₂S₄ hollow sub-microspheres with mesoporous nanoshells support Pd nanoparticles for enhanced hydrogen evolution reaction electrocatalysis in both acidic and alkaline conditions, *ACS Appl. Mater. Interfaces* 10 (2018) 22248–22256, <https://doi.org/10.1021/acsami.8b05427>.
- [18] H. Chen, M. Yuan, C. Zhai, L. Tan, N. Cong, J. Han, H. Fang, X. Zhou, Z. Ren, Y. Zhu, Nano PdFe alloy assembled film as a highly efficient electrocatalyst toward hydrogen evolution in both acid and alkaline solutions, *ACS Appl. Energy Mater.* 3 (2020) 8969–8977, <https://doi.org/10.1021/acsaelm.0c01410>.
- [19] J. Guo, L. Gao, X. Tan, Y. Yuan, J. Kim, Y. Wang, H. Wang, Y.J. Zeng, S.I. Choi, S. C. Smith, H. Huang, Template-directed rapid synthesis of Pd-based ultrathin porous intermetallic nanosheets for efficient oxygen reduction, *Angew. Chem., Int. Ed.* 60 (2021) 10942–10949, <https://doi.org/10.1002/anie.202100307>.
- [20] Y. Ge, J. Ge, B. Huang, X. Wang, G. Liu, X.-H. Shan, L. Ma, B. Chen, G. Liu, S. Du, A. Zhang, H. Cheng, Q. Wa, S. Lu, L. Li, Q. Yun, K. Yuan, Q. Luo, Z.J. Xu, Y. Du, H. Zhang, Synthesis of amorphous Pd-based nanocatalysts for efficient alcoholysis of styrene oxide and electrochemical hydrogen evolution, *Nano Res* (2022) 1–6, <https://doi.org/10.1007/s12274-022-5101-0>.
- [21] Y. Teng, K. Guo, D. Fan, H. Guo, M. Han, D. Xu, J. Bao, Rapid aqueous synthesis of large-size and edge/defect-rich porous Pd and Pd-alloyed nanomesh for electrocatalytic ethanol oxidation, *Chem. - A Eur. J.* 27 (2021) 11175–11182, <https://doi.org/10.1002/chem.202101144>.
- [22] F. Lv, B. Huang, J. Feng, W. Zhang, K. Wang, N. Li, J. Zhou, P. Zhou, W. Yang, Y. Du, S. Guo, A highly efficient atomically thin curved PdRh bimetallic electrocatalyst, *nwb019*, *Nati. Sci. Rev.* 8 (2021), <https://doi.org/10.1093/nsr/nwab019>.
- [23] K. Yan, T. Wei, H. Ren, J. Wu, X. Pan, X. Xu, L. Liu, X. Wu, Asymmetric exchange interaction induces highly efficient alkaline hydrogen evolution in RhFe bimetallic, *Small* 18 (2022) 2204456, <https://doi.org/10.1002/sml.202204456>.
- [24] Q. Mao, P. Wang, Z. Wang, Y. Xu, X. Li, L. Wang, H. Wang, PdRh bimetallic for energy-saving hydrogen production via methanol electroreforming, *Appl. Mater. Today* 26 (2022), 101400, <https://doi.org/10.1016/j.apmt.2022.101400>.
- [25] S. Wang, F. Wang, H. Liu, H. Huang, X. Meng, Y. Ouyang, M. Jiang, T. Zeng, H. Chen, L. Zheng, L.Y. Zhang, Defective PdRh bimetallic nanocrystals enable enhanced methanol electrooxidation, *Colloid Surf. A* 616 (2021), 126323, <https://doi.org/10.1016/j.colsurfa.2021.126323>.
- [26] K. Deng, Q. Mao, W. Wang, P. Wang, Z. Wang, Y. Xu, X. Li, H. Wang, L. Wang, Defect-rich low-crystalline Rh metallene for efficient chlorine-free H₂ production by hydrazine-assisted seawater splitting, *Appl. Catal. B: Environ.* 310 (2022), 121338, <https://doi.org/10.1016/j.apcatb.2022.121338>.
- [27] Y. Zhao, N. Jia, X.-R. Wu, F.-M. Li, P. Chen, P.-J. Jin, S. Yin, Y. Chen, Rhodium phosphide ultrathin nanosheets for hydrazine oxidation boosted electrochemical water splitting, *Appl. Catal. B: Environ.* 270 (2020), 118880, <https://doi.org/10.1016/j.apcatb.2020.118880>.
- [28] Peng Xingchuan Li, Yaojing Shen, Yunhe Luo, Yali Li, Guo, K.Chu Hu Zhang, PdFe single-atom alloy metallene for N₂ electroreduction, *Angew. Chem., Int. Ed.* 61 (2022), e202205923, <https://doi.org/10.1002/ange.202205923>.
- [29] J. Fan, Z. Feng, Y. Mu, X. Ge, D. Wang, L. Zhang, X. Zhao, W. Zhang, D.J. Singh, J. Ma, L. Zheng, W. Zheng, X. Cui, Spatially confined PdH_x metallenes by tensile strained atomic Ru layers for efficient hydrogen evolution, *J. Am. Chem. Soc.* 145 (2023) 5710–5717, <https://doi.org/10.1021/jacs.2c11692>.
- [30] K. Chen, Z. Ma, X. Li, J. Kang, D. Ma, K. Chu, Single-atom Bi alloyed Pd metallene for nitrate electroreduction to ammonia, *Adv. Funct. Mater.* (2023) 2209890, <https://doi.org/10.1002/adfm.202209890>.
- [31] Z. Wang, S. Xu, M. Li, K. Deng, H. Yu, Y. Xu, X. Li, H. Wang, L. Wang, Polyethyleneimine-functionalized PdOs bimetallic for enhanced oxygen reduction, *Chem. Commun.* 59 (2023) 4511–4514, <https://doi.org/10.1039/d3cc00221g>.
- [32] J. Fan, J. Wu, X. Cui, L. Gu, Q. Zhang, F. Meng, B.-H. Lei, D.J. Singh, W. Zheng, Hydrogen stabilized RhPdH₂ 2D bimetallic nanosheets for efficient alkaline hydrogen evolution, *J. Am. Chem. Soc.* 142 (2020) 3645–3651, <https://doi.org/10.1021/jacs.0c00218>.
- [33] X. Li, P. Shen, X. Li, D. Ma, K. Chu, Sub-nm RuO_x clusters on Pd metallene for synergistically enhanced nitrate electroreduction to ammonia, *ACS Nano* (2023), <https://doi.org/10.1021/acsnano.2c07911>.
- [34] J. Wu, J. Fan, X. Zhao, Y. Wang, D. Wang, H. Liu, L. Gu, Q. Zhang, L. Zheng, D. J. Singh, X. Cui, W. Zheng, Atomically dispersed MoO_x on rhodium metallene boosts electrocatalyzed alkaline hydrogen evolution, *e202207512*, *Angew. Chem., Int. Ed.* 61 (2022), <https://doi.org/10.1002/ange.202207512>.
- [35] M. Luo, Z. Zhao, Y. Zhang, Y. Sun, Y. Xing, F. Lv, Y. Yang, X. Zhang, S. Hwang, Y. Qin, J.-Y. Ma, F. Lin, D. Su, G. Lu, S. Guo, PdMo bimetallic for oxygen reduction catalysis, *Nature* 574 (2019) 81–85, <https://doi.org/10.1038/s41586-019-1603-7>.
- [36] K. Deng, W. Wang, Q. Mao, H. Yu, Z. Wang, Y. Xu, X. Li, H. Wang, L. Wang, Boron-intercalation-induced phase evolution of Rh metallene for energy-saving H₂ production by H₂O₂ oxidation coupled with water electrolysis, *Small* 18 (2022) 2203020, <https://doi.org/10.1002/sml.202203020>.
- [37] N. Yang, H. Cheng, X. Liu, Q. Yun, Y. Chen, B. Li, B. Chen, Z. Zhang, X. Chen, Q. Lu, J. Huang, Y. Huang, Y. Zong, Y. Yang, L. Gu, H. Zhang, Amorphous/crystalline hetero-phase Pd nanosheets: one-pot synthesis and highly selective hydrogenation reaction, *Adv. Mater.* 30 (2018) 1803234, <https://doi.org/10.1002/adma.201803234>.
- [38] J. Ge, D. He, W. Chen, H. Ju, H. Zhang, T. Chao, X. Wang, R. You, Y. Lin, Y. Wang, J. Zhu, H. Li, B. Xiao, W. Huang, Y. Wu, X. Hong, Y. Li, Atomically dispersed Ru on ultrathin Pd nanoribbons, *J. Am. Chem. Soc.* 138 (2016) 13850–13853, <https://doi.org/10.1021/jacs.6b09246>.
- [39] L. Tao, M. Sun, Y. Zhou, M. Luo, F. Lv, M. Li, Q. Zhang, L. Gu, B. Huang, S. Guo, A general synthetic method for high-entropy alloy subnanometer ribbons, *J. Am. Chem. Soc.* 144 (2022) 10582–10590, <https://doi.org/10.1021/jacs.2c03544>.
- [40] H. Yu, T. Zhou, Z. Wang, Y. Xu, X. Li, L. Wang, H. Wang, Defect-rich porous palladium metallene for enhanced alkaline oxygen reduction electrocatalysis, *Angew. Chem., Int. Ed.* 60 (2021) 12027–12031, <https://doi.org/10.1002/ange.202101019>.
- [41] S. Zhang, K. Liu, Z. Liu, M. Liu, Z. Zhang, Z. Qiao, L. Ming, C. Gao, Highly strained Au-Ag-Pd alloy nanowires for boosted electrooxidation of biomass-derived alcohols, *Nano Lett.* 21 (2021) 1074–1082, <https://doi.org/10.1021/acs.nanolett.0c04395>.
- [42] S. Liu, H. Ren, S. Yin, H. Zhang, Z. Wang, Y. Xu, X. Li, L. Wang, H. Wang, Defect-rich ultrathin AuPd nanowires with boerdijk-coxeter structure for oxygen reduction electrocatalysis, *Chem. Eng. J.* 435 (2022), 134823, <https://doi.org/10.1016/j.cej.2022.134823>.
- [43] M. Li, Z. Zhao, Z. Xia, M. Luo, Q. Zhang, Y. Qin, L. Tao, K. Yin, Y. Chao, L. Gu, W. Yang, Y. Yu, G. Lu, S. Guo, Exclusive strain effect boosts overall water splitting in PdCu/Ir core/shell nanocrystals, *Angew. Chem., Int. Ed.* 60 (2021) 8243–8250, <https://doi.org/10.1002/ange.202016199>.
- [44] S. Liu, S. Yin, Z. Wang, Y. Xu, X. Li, L. Wang, H. Wang, AuCu nanofibers for electrosynthesis of urea from carbon dioxide and nitrite, *Cell Rep. Phys. Sci.* 3 (2022), 100869, <https://doi.org/10.1016/j.xcrp.2022.100869>.
- [45] F. Lin, F. Lv, Q. Zhang, H. Luo, K. Wang, J. Zhou, W. Zhang, W. Zhang, D. Wang, L. Gu, S. Guo, Local coordination regulation through tuning atomic-scale cavities of Pd metallene toward efficient oxygen reduction electrocatalysis, *Adv. Mater.* 34 (2022) 2202084, <https://doi.org/10.1002/adma.202202084>.

- [46] Q. Mao, S. Jiao, K. Ren, S. Wang, Y. Xu, Z. Wang, X. Li, L. Wang, H. Wang, Transition metal and phosphorus co-doping induced lattice strain in mesoporous Rh-based nanospheres for pH-universal hydrogen evolution electrocatalysis, *Chem. Eng. J.* 426 (2021), 131227, <https://doi.org/10.1016/j.cej.2021.131227>.
- [47] R. Zhang, Y. Zhao, Z. Guo, X. Liu, L. Zhu, Y. Jiang, Highly selective Pd nanosheet aerogel catalyst with hybrid strain induced by laser irradiation and P doping postprocess, *Small* 19 (2022) 2205587, <https://doi.org/10.1002/smll.202205587>.
- [48] S. Han, C. Wang, Y. Wang, Y. Yu, B. Zhang, Electrosynthesis of nitrate via the oxidation of nitrogen on tensile-strained palladium porous nanosheets, *Angew. Chem., Int. Ed.* 60 (2021) 4474–4478, <https://doi.org/10.1002/anie.202014017>.
- [49] H. Shang, H. Xu, L. Jin, C. Chen, C. Wang, T. Song, Y. Du, Three-dimensional palladium-rhodium nanosheet assemblies: Highly efficient catalysts for methanol electrooxidation, *J. Colloid Interf. Sci.* 556 (2019) 360–365, <https://doi.org/10.1016/j.jcis.2019.08.076>.
- [50] L. Jin, H. Xu, C. Chen, H. Shang, Y. Wang, C. Wang, Y. Du, Three-dimensional PdCuM (M = Ru, Rh, Ir) trimetallic alloy nanosheets for enhancing methanol oxidation electrocatalysis, *ACS Appl. Mater. Interfaces* 11 (2019) 42123–42130, <https://doi.org/10.1021/acsami.9b13557>.
- [51] Y. Li, C.-K. Peng, H. Hu, S.-Y. Chen, J.-H. Choi, Y.-G. Lin, J.-M. Lee, Interstitial boron-triggered electron-deficient Os aerogels for enhanced pH-universal hydrogen evolution, *Nat. Commun.* 13 (2022) 1143, <https://doi.org/10.1038/s41467-022-28805-8>.
- [52] D. Wang, X. Jiang, Z. Lin, X. Zeng, Y. Zhu, Y. Wang, M. Gong, Y. Tang, G. Fu, Ethanol-induced hydrogen insertion in ultrafine IrPdH boosts pH-universal hydrogen Evolution, *Small* 18 (2022) 2204063, <https://doi.org/10.1002/smll.202204063>.